

Passive Drag Reduction Optimization for Complex Commercial Vehicle Models

G. Liao¹, M. Xue¹, L. Yue¹, H. Yang¹, P. Guo², X. Hu², Z. Wang^{2†} and T. Ma²

¹ FAW Liberation Co., Ltd. Commercial Vehicle Development Institute, Changchun 130000, China

² State Key Laboratory of Automotive Simulation and Control, Jilin University, Changchun 130022, China

†Corresponding Author Email: wangzr22@mails.jlu.edu.cn

ABSTRACT

The long-distance transportation of heavy commercial vehicles is facing increasing pressure. Low wind resistance and low fuel consumption will become the objective requirements and development trend of heavy commercial vehicles. In this paper, the 1:1 complex model of commercial vehicle is taken as the research object to study the passive drag reduction of the commercial vehicle. First, simulation analysis is conducted, and then the wind tunnel test of the 1:2.5 complex model is performed to verify the accuracy of the simulation scheme and results. Then, the geometric shape of the cab is parameterized and controlled by 13 parameters. After determining the range of parameter changes, Latin hypercube sampling is selected, and large eddy simulation is used for numerical simulation to construct the sample space. Taking the shape parameter as the input factor and the coefficient of drag C_D as the target response, the initial surrogate model is constructed, and the sample points are supplemented by the combination of global and local point addition strategies to improve the accuracy of the surrogate model. Finally, $R^2=0.812$. The local details of the optimization results are optimized, and the low-wind-resistance shapes of the cabs of the three styling styles are obtained. Among them, the bullet model has the lowest C_D . Compared with the basic model, the drag reduction rate is 28%, and the coefficient of drag is simulated. The error between the value and the test value is within 1%.

Article History

Received July 25, 2024

Revised January 2, 2025

Accepted January 6, 2025

Available online March 30, 2025

Keywords:

Aerodynamic characteristics

PSO algorithm

Surrogate model

Vehicle shape optimization

1. INTRODUCTION

1.1 Research Significance

Global energy supply is facing increasingly severe challenges. Heavy-duty commercial vehicles usually rely on petroleum fuels, while petroleum resources are limited and nonrenewable. With the growth of energy demand and the fluctuation of oil price, reducing the energy consumption of commercial vehicles has become crucial. With the improvement of environmental awareness and concerns about climate change, many countries and regions have adopted laws and regulations to limit greenhouse gas emissions. The Conference of the Parties (COP) is an international negotiating body under the United Nations Framework Convention on Climate Change. COP 28 aims to develop a global climate action plan to address climate change and to reduce greenhouse gas emissions. Drag reduction research on commercial vehicles can help achieve the COP 28 goal of mitigating the effects of climate change by reducing carbon emissions.

A car traveling is subject to air resistance, the magnitude of which is related to the coefficient of drag. When the coefficient of drag is reduced, the air resistance decreases

when the air density, vehicle speed and windward area remain unchanged. Car engine to output power to overcome the driving resistance, including air resistance, resistance is reduced, according to the power formula, in the speed of the same, the engine output power is reduced. Fuel consumption rate refers to the engine every 1kW of power in 1 hour of fuel consumption, the engine power is reduced, the same driving conditions per unit of time the amount of fuel burned will be reduced, thus reducing the fuel consumption rate. According to a study by Wiedemann in 1996, every 10 per cent reduction in the drag coefficient of a vehicle multiplied by the windward surface area reduces fuel consumption by an average of 3 per cent, according to the standards of the European Commission's Engine Vehicle Emissions Group (Wiedemann, 1996). According to the data of the European Commission, in 2010, an average of 23.9% of the commercial vehicle kilometers are no-load driving (European Commission- DG Transport 2013). In no-load driving, air resistance accounts for a higher proportion of fuel consumption, especially in long-distance transportation conditions. The air resistance fuel consumption ratio of 40000 and 20000 kg flat-headed vehicles in long-haul driving cycles long-distance driving

Nomenclature		
Co	Courant number	$u(x)$ global trend function
\mathcal{C}^T	sample point function values linear superposition weight coefficient matrix	$v_i(k)$ velocity of the I-th particle at the Kth iteration
c_1, c_2	learning factor	w_0/w_i polynomial coefficients to be estimated
$c_{1i}, c_{1f}, c_{2i}, c_{2f}$	constant	ω inertia weight
g_{best}	global extreme value	Δx grid size
iter	current number of iterations	x_i sample i
MSE	Mean Square Error	x^* normalized data
MAXITER	maximum number of iterations	$x_i(k)$ position of the I-th particle at the Kth iteration
p_{ibest}	individual extreme value	$\hat{y}(x)$ predicted value
R	correlation coefficient matrix	$Y(x)$ Gaussian process
r	correlation coefficient vector	Y sample response value
rand ()	random number between [0, 1]	\hat{y}_{-i} remove the i th point to construct the predicted value of the proxy model
Δt	time step	$Z(x)$ standard normal distribution
U	fluid velocity	

conditions accounts for 38.2% and 52.1%, respectively (Mohamed-Kassim & Filippone, 2010). According to the Transportation Energy Data Book, Edition 40, June 2022 statistics, if calculated by oil, based on heavy truck 2977 k barrels of oil/day (a barrel of 42 gallons) at \$ 80 per barrel (Davis & Boundy 2022), heavy truck aerodynamic drag is reduced by 10%, fuel consumption is reduced by 3%, 1.4 billion gallons of oil can be saved, 12 million tons of carbon dioxide emissions can be reduced, and \$ 2.6 billion/year can be saved. In summary, studying the drag reduction of commercial vehicles is important because it can promote sustainable transportation development, reduce energy consumption and carbon emissions, improve fuel efficiency, reduce operating costs, and help achieve the requirements of laws and regulations and international climate goals. Moreover, the research on drag reduction of commercial vehicles can advance the development and innovation of related technologies and provide sustainable, more environmentally friendly solutions for the future transportation field.

1.2 Summary of Drag Reduction Methods for Commercial Vehicles

The existing drag reduction research of heavy commercial vehicles focuses on two aspects: active drag reduction and passive drag reduction. Active drag reduction is also known as active flow control. The control system only works when the flow needs to be controlled. Zhang et al. (2020) set up jet ports in several locations of the MIRA body to achieve jet blowing, and confirmed the drag reduction effect of local jets by comparing the drag coefficients, surface static pressure coefficients, and directional vortices with those in the original model of the MIRA. Finally, the aerodynamic drag coefficient was reduced by 16.3%. Wang et al. (2020) added a surface dielectric barrier discharge-based plasma actuator to the tail section of a square-backed Ahmed model to study the control effect of the tail section separation flow, and the plasma actuator can effectively control the tail section flow, improve the tail section pressure. The plasma actuator can effectively control the tail flow and improve the tail pressure of the model, and the active drag reduction rate is as high as 4.58%. Currently, active drag reduction

technology for commercial vehicles is not widely used, because the main disadvantage of active flow control is that the system needs power to function, which increases the power consumption of the vehicle. In contrast, the passive drag reduction method uses an additional shape that influences the flow field on the vehicle body, which has an ideal effect on drag reduction. Compared with the active drag reduction device, most of the passive drag reduction methods have a simple structure, no additional energy consumption, and a high return rate. Yadegari et al. (2023) studied the effect of wake characteristics by using trip wires, spiral strips etc. on simple cylinders and the drag coefficients were significantly reduced by up to 75% (Yadegari & Bak Khoshnevis, 2021). Therefore, the research direction of this paper is passive drag reduction. Some existing studies have proven that the shape of commercial vehicles still has the potential of low-wind-resistance optimization. Levin and Chen (2023) studied three kinds of shroud add-on designs (REF-A, REF-B, and REF-C) for high-pressure concentrated pocket areas of commercial vehicles, redirecting the incoming fluid to the side of the truck and preventing the formation of high-pressure areas in the pocket area to reduce air resistance. The optimal design reduces the aerodynamic drag by 16.5%. Kim and Kim (2023) studied the influence of the cab expander installed at the rear of the cab on the drag coefficient of commercial vehicles through wind tunnel tests and CFD. The cab extender significantly changes the flow structure around the vehicle, reducing the wind resistance by 8.2 per cent compared to the original model. Farghaly et al. (2023) used a standard heavy truck 1/50 scale to construct a calculation and test model, and added various drag reduction devices (truck caps with different angles, clearance devices with different lengths, and flat flaps with different angles and sizes) to improve the vehicle profile. The results showed that installing all auxiliary components simultaneously helps reduce the drag coefficient by about 59%. Garcia-Ribeiro et al. (2023) highlighted the lack of drag reduction devices for commercial buses. In this article they show three different devices, large eddy current generators, side devices with NACA upper surfaces, and roof rails with inclined notches. Together these devices reduced drag by 8.6%. Aleksandra

and Alvin (2022) modified the trailing edge of a heavy truck to look like a bladed mixer and compared it to a simple 15° tapered trailing edge. The mixer design reduced drag by 7 per cent, while the tapered design reduced it by 10.8 per cent. McAuliffe et al. (2022) explored the aerodynamic effects of heavy truck modifications using a 30% scale model in a large wind tunnel facility. Removing mirrors reduced drag by 4%. Optimising the shape of the tractor cab reduced drag by 7-9%. Side skirts reduced drag by about 7 per cent, while the addition of a small boat tail reduced the drag of the skirt by 10-11 per cent. Bayindirli (2021) proposed a new type of drag reduction device for buses with a semi-cylindrical rod placed in front of the bus, which achieved up to 10 per cent drag reduction after testing different diameters of cylinders. Arabacı and Pakdemirli (2023) were inspired by the whale, designing the front area of a bus, several model variants simulating a beluga whale were proposed. The new beluga design is expected to reduce fuel consumption by 12.64 per cent.

For complex real vehicle models, most of the research can only be designed based on the experience of engineers, and shape optimization requires a large amount of calculation and evaluation. Wind tunnel tests require numerous deformation models, and the cost is extremely high. Therefore, CFD is used more frequently in the early stage. The solution of a grid example of the order of 3 kw requires about 800 cores. If it is iterated hundreds of times according to the traditional optimization, it cannot be achieved in practical applications. Engineering optimization design based on surrogate model emerges as the times require. Sample points are extracted through experimental design, and finite initial sample points are numerically simulated. An efficient approximate numerical model is established to replace the time-consuming numerical simulation. This method has been widely used in the field of aerodynamic shape optimization of wing airfoils, and some simplified vehicle model optimization studies have also been applied. Wang et al. (2017) studied the drag reduction of no smooth surfaces through a simplified armed model and determined the optimal combination based on the Kriging surrogate model to reduce the aerodynamic drag coefficient by 5.20%. Magnus Urquhart used Windsor to simplify the passenger car model, used optimized Latin square sampling, and used the radial basis surrogate model to optimize the tail flap angle. The optimization results of the surrogate model are verified by experiment.

However, most optimizations based on surrogate models are only applicable to simple models or 2D shapes. First, simple models are easier to parameterize. Second, with fewer input variables, the dimension of the surrogate model the lower, fewer samples are required to establish the surrogate model, and achieving high accuracy is easier. Therefore, most of the existing commercial vehicle low-drag optimization studies use simplified models, and studies on complex real vehicle optimization are few. As shown in Fig. 1, there are fewer studies on the optimisation of complex real vehicles due to the large number of internal system parts and the complexity of the shape compared to the simple model, and the results are not universal. This paper uses the actual commercial vehicle 1:1 complex model, controls the cab shape through 13 shape parameters, and establishes a high-dimensional adaptive surrogate model to replace many numerical

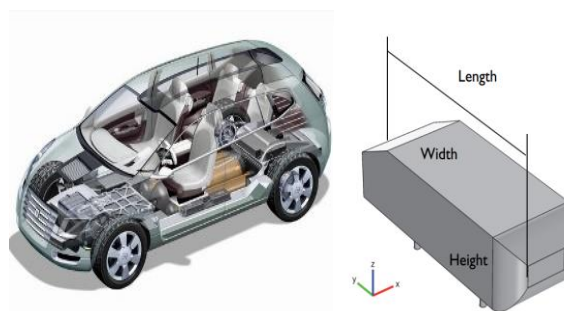


Fig. 1 Real car and Ahmed model

Table 1 Conditions for numerical simulation

typology	Parameter
Turbulence model	Realizable k-epsilon/ LES
mesh type	Trimmer mesh
outlet boundary condition	standard atmospheric pressure
Inlet boundary conditions	25m/s
flow type	Segregated flow
convection term discrete	2n-order

simulations. The input variables are constrained to control the cab shape of different styles, and the minimum wind resistance results of diverse types of cabs are obtained by multiple rounds of iteration. The conditions for numerical simulation are shown in Table 1. Finally, the 1:2.5 optimization model is processed to verify the optimization results through wind tunnel tests. Due to the different scale sizes of the models used for simulation and experiment, in this paper, we consider the Reynolds number to be unchanged and correct the results according to the similarity criterion, which will be presented in the third part.

2. RESEARCH METHOD

2.1 Numerical Simulation Strategy

Considering the use of complex real vehicle models, the Reynolds- average Navier-Stokes equation (RANS) solution has limitations and is not applicable to the solution of complex flows. Direct numerical simulation (DNS): Although the solution is the most accurate, it has a high demand for spatial and temporal resolution, so it is computationally intensive, time consuming, and highly dependent on computer performance. Therefore, in this paper, the large eddy simulation method is used to solve the Navier–Stokes equation on unstructured grids using the WALE sub grid scale model (You & Moin, 2009). The model boundary conditions are shown in Fig. 2.

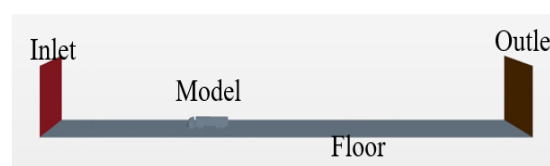
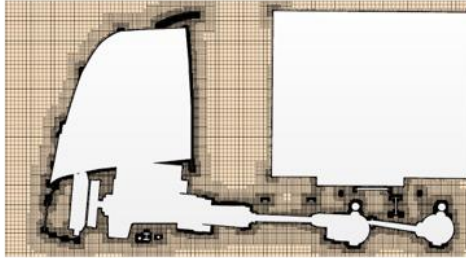


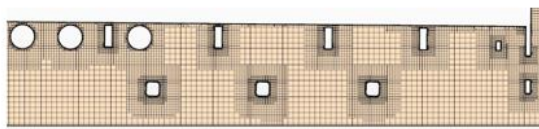
Fig. 2 Boundaries of model simulation



(a) Overall grid diagram



(b) Position ① Enlarge the picture



(c) Position ② Enlarge the picture

Fig. 3 Grid XOZ cross section

$$Co = \frac{U\Delta t}{\Delta x} \quad (1)$$

Equation u is the fluid velocity; Δt is the time step; Δx is the grid size. The minimum mesh size of the model surface is 5 mm, and the final total number of meshes is about 3100 w. The mesh section is shown in Fig. 3. [Aultman et al. \(2021\)](#) performed CFD simulations of the driver fastback model and showed that only when the CFL was increased from 1 to 100, the CD between CFD and wind tunnel experiments showed a large deviation (about 2.1%). On the contrary, the obtained mean surface pressure coefficients, mean velocities and wake flows remain similar when CFL= 50 and CFL=1. Therefore, considering time and accuracy, CFL= 5 is chosen in this paper. The second-order discrete accuracy is used for the time, and the time step is 0.001 s. The computational domain is 3 times the length of the front car, 7 times the length of the rear car, 6 times the width of the car, and 6 times the height of the car. The computational domain walls are symmetric planes, with slip walls for large floors and tangential velocity non-slip walls for small floors, to more realistically simulate the near-surface flow state of the car. The model boundary conditions are shown in Fig. 4. The velocity inlet is used, the wind speed is 25 m/s, and the Re is 1.7×10^7 . The first 5000 steps of steady-state calculation are helpful for the convergence of transient calculation, and the physical time of transient calculation is 8 s.

2.2 Optimization Method Based on Surrogate Model

Before establishing the surrogate model, a sufficient number of sample spaces must be established. How to achieve greater results at the minimum cost is what Design of Experiments (DOE) studies. DOE first evaluates the

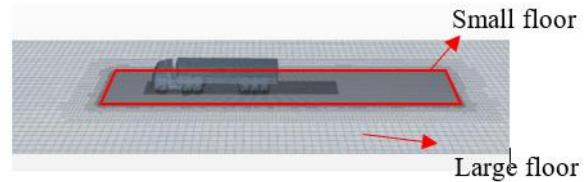
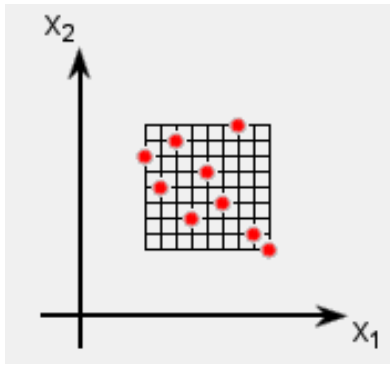


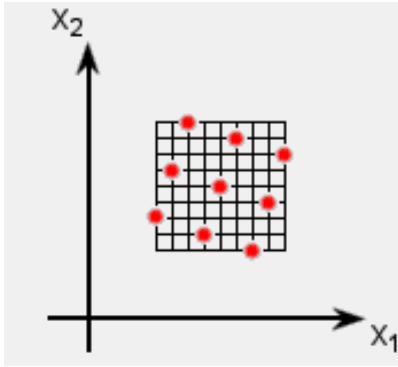
Fig. 4 Range of sliding and non-sliding floors

influence of input parameters on output parameters, identifies important parameter interactions, eliminates factors that have a minor effect on output, analyzes the design space and estimates the optimal design, and uses the sampling strategy to construct a sample space for generating the surrogate model. For the high dimensional sampling in this paper, it is clear that full factorial sampling, which produces dimensional catastrophes, cannot be used. Three scholars such as [McKay et al. \(2020\)](#) in North America first proposed the Latin hypercube sampling method in 1979 and further developed and improved it. This sampling method controls the selection position of sample points in the sample space, which can avoid the defect that the sample points overlap in a small area. The principle of this method is to divide n random variables into k equal probability intervals if k times of sampling are needed, and the sampling space is divided into $k * n$ equal probability regions. For any variable R , k times of sampling fall in the divided regions, and the sampling points also fall in the whole sampling space. However, due to the randomness of sampling, the test combination quality of the Latin hypercube sampling method does not possess satisfactory robustness, that is, the resulting test scheme cannot guarantee a uniform full sampling space. On this basis, the Latin hypercube sampling method is optimized, and the relevant rules are added to make the horizontal distribution of the sample points in the design matrix uniform. The Latin hypercube sampling method and the optimized Latin hypercube sampling method are shown in Fig. 5. Due to the above advantages, this paper uses the optimized Latin hypercube sampling method for experimental design.

Surrogate model, in engineering design, approximates the complex real model to reduce calculations. The surrogate model is a mathematical modeling method that can interpolate or fit complex engineering systems of different dimensions at a faster computing speed based on a certain number of existing data information. At present, agent model technology has been widely used in mechanical design, electronic design, aerospace, artificial intelligence, and other fields ([Lv et al., 2024](#)). However, for complex engineering problems, a single-agent model usually does not meet the requirements, and determining what type of agent model is most suitable for specific engineering problems is difficult. How to select the appropriate agent model is also a problem. Hence, the combined agent model technology emerged. The combined surrogate model selects various kinds of surrogate models for specific problems. Compared with the single-agent model, the combined-agent model directly weights the candidate set of the agent model, which saves much time spent on screening the agent model, the accuracy of the combined agent model is generally higher than that of the single agent model, and the robustness is better.



(a) Latin hypercube sampling method



(b) Optimized Latin hypercube sampling method

Fig. 5 Schematic diagram of Latin hypercube and optimized Latin hypercube sampling method

In this paper, the polynomial response surface and the Kriging KRG surrogate model are weighted. The response surface is one of the simplest surrogate models, and the quadratic polynomial is commonly used. The essence is to construct a multivariate n -order equation, so a minimum number of sample points exists (less than this number, the equation constructed is not unique, and the number of samples is equal to the number of samples passing through all sample points), but the actual number of sample points is mostly larger than the number. Hence, it must be fitted by the least square method, so it does not necessarily pass through the sample points. The main parameter is the polynomial degree. Taking the second-order response surface model as an example, the low-order response surface model describes the gentle terrain and can better restore the overall trend.

$$\hat{y}(x) = w_0 + \sum_{i=1}^n w_i x_i + \sum_{i=1}^n \sum_{j=i+1}^n w_{ij} x_i x_j \quad (2)$$

w_0 and w_i are the polynomial coefficients to be estimated; n is the number of independent variables. The Kriging model is more suitable for high-dimensional nonlinear problems. The principle is that the original problem is regarded as a normal random process, that is, a Gaussian process, expressed as follows:

$$Y(x) = u(x) + Z(x) \quad (3)$$

$u(x)$ is a global trend function, which represents the expected value of a normal random process. It can be a constant or a polynomial with x as an independent variable. When $u(x)$ is a constant, the model is called simple Kriging (SK). $Z(x)$ is a stationary random process with mean value of 0 and variance of σ^2 . When $u(x)$ is a

polynomial, the solved model is called universal Kriging (UK). Therefore, the mean value of $Y(x)$ is u , and the variance is σ^2 .

In order to satisfy the unbiasedness, there are

$$E[\hat{y}(x)] = E[C^T Y] = E[y(x)] \quad (4)$$

In order to minimize mean square error

$$MSE [\hat{y}(x)] = E[(C^T Y - y(x))^2] \quad (5)$$

It can be transformed into an optimization problem

$$\begin{aligned} \min \quad & \text{obj} = \sigma^2(1 + C^T R C - 2C^T r) \\ \text{s.t.} \quad & C^T 1 - 1 = 0 \end{aligned} \quad (6)$$

In Equation 4-6, R is the matrix of correlation coefficients between sample points, r is the vector of correlation coefficients between predicted and known points. c is the matrix of linearly superimposed weight coefficients of the function values of the sample points, y is the sample response value, and $\hat{y}(x)$ is the predicted value of the agent model.

The accuracy verification of the model mainly includes two aspects: the verification of global accuracy and local accuracy. The global accuracy evaluation criteria are mainly composed of two kinds, namely, root mean square error (RMSE) (Willmott & Matsuura, 2005) and coefficient of determination (R^2) (Nagelkerke, 1991), expressed as follows:

$$RMSE = \sqrt{\frac{1}{n} \sum_{i=1}^n (y_i - \hat{y}_i)^2} \quad (7)$$

$$R^2 = 1 - \frac{\sum_{i=1}^n (y_i - \hat{y}_i)^2}{\sum_{i=1}^n (y_i - \bar{y})^2} \quad (8)$$

At present, the most widely used combined surrogate model prediction accuracy evaluation index is the predicted error sum of square (PRESS) (Schiavo et al., 2009). The PRESS value can be calculated by cross-validation (CV) (Bates et al., 2023), so that no resampling is needed as the prediction point, which saves the calculation cost. CV is divided into the leave-one-out method and the k -fold method. To evaluate the importance of each sample point for modeling, five-fold CV is selected as the prediction accuracy verification method.

$$e_i = y_i - \hat{y}_{-i} \quad (9)$$

The specific calculation of the PRESS value is that when n sample points are in the database, all sample points except the i_{th} point are used to construct the surrogate model, and the i_{th} point is used as the prediction point of the surrogate model. The prediction error corresponding to the sample point i is expressed as follows:

$$PRESS = \sum_{i=1}^n e_i^2 \quad (10)$$

Among the three most widely used methods for constructing the combined proxy model, the most classic one is to use the PRESS value as a measure of the weight coefficient calculation. If the PRESS value of a proxy model is larger, the weight coefficient is smaller. This approach is also called the inverse proportional averaging method, and its weight coefficient is calculated as follows:

$$\omega_i = \frac{\frac{1}{P_i}}{\sum_{j=1}^N \frac{1}{P_j}} \quad (11)$$



Fig. 6 Model simplification

3. WIND RESISTANCE SHAPE OPTIMIZATION BASED ON SURROGATE MODEL

3.1 Model Processing and Shape Parameterization

A commercial vehicle in China First Automobile Works (FAW) is split, and a complex model of the vehicle is constructed by 3d scanning technology. The geometric cleaning is conducted by ANSA. The structure that has a slight influence on the CFD results and is not conducive to the convergence of numerical calculation is removed and simplified. The treatment of the cab includes the removal of the antenna, the top shroud bracket, the sunshade, the view mirror combination, the vehicle logo, the wiper, and the front wind window external handle and the simplification of the cab top pattern and shape, the front side shape line, the front grille, and the front protection shape. The trailer processing includes simplifying the trailer front profile light, trailer side department and hinge, trailer rear department, hinge, and license plate; the chassis removes the wiring harness to retain most of the parts and simplifies the modeling of each part. The tire simplifies the tread and performs the closed hub treatment. The comparison of model processing is shown in Fig. 6.

For the base model, the $k-\epsilon$ turbulence model is adopted. The model is preliminarily simulated according to the inlet velocity of 25 m/s and the boundary condition of standard atmospheric pressure outlet, and the steady-state calculation is 5000 steps. Subsequent transient calculations were performed with a step size of 0.001s, and the total calculation time totaled 8s. The pressure distribution of the base model is shown in Fig. 7. The pressure distribution of the middle section shows two high-pressure areas. The first is the front grille, which extends to the connection between the engine hood and the front wind window. The second is the front side of the top shroud. Because the front grille is the front end of the windward side of the vehicle, the pressure coefficient here is higher. From the front view, the high-pressure area is mainly in the grille area, the lower part of the front wind window, and the windward side of the front wheel. Because the front shape is straight and excessively rigid, the y direction of the front high-pressure area is larger. The low-pressure area on the side is in the fender, front side window, and wheel area. Therefore, the windward side needs to focus on the excessive inclination of the front wall, the wind window, and the ceiling and the excessive fillet between the front face and the side. The airflow of the

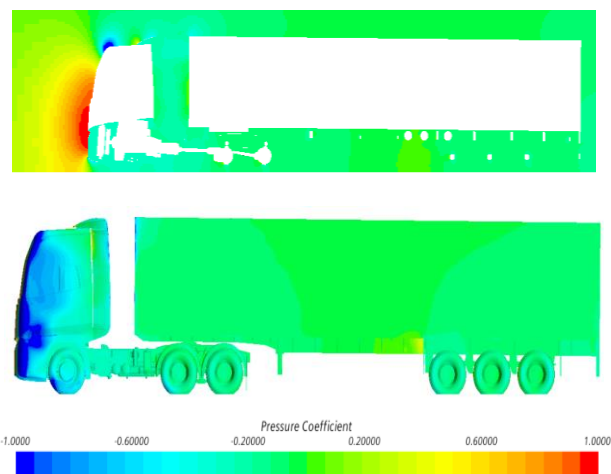


Fig. 7 Vehicle pressure coefficient distribution

ceiling dome rises upward, and a separation exists along the way. The shape of the top of the cab and the dome need to be optimized.

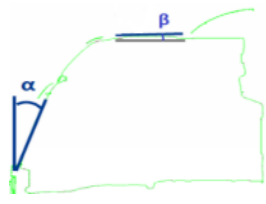
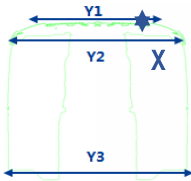
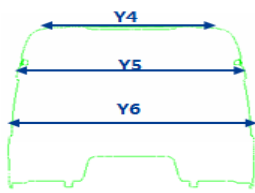
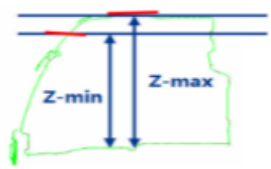
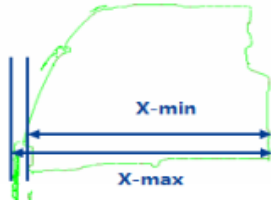
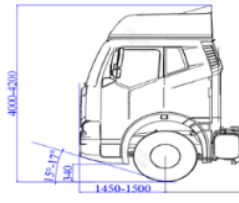
Combined with the above simulation results and the geometric characteristics analysis of the cab model, it is mainly divided into length, width, height characteristics, and windward inclination characteristics. Specifically, it includes wind window inclination angle, ceiling inclination angle, side wall rotation angle, cab front wall width characteristics, cab wind window width characteristics, cab height characteristics, cab length characteristics, and front suspension length characteristics. The deformation illustration is shown in Table 2. For the determination of the range of deformation parameters, ergonomics, such as the driver's eye ellipse, must first be considered to reflect the rationality of deformation fully, to ensure the driver's riding space, consider the layout of body parts and other factors, be consistent with the existing automobile manufacturing process, facilitate producing the surface of the existing process, combine with the laws and regulations of the external size restrictions, consider the determination of the range of deformation parameters, and according to the numerical value of the parameters determine the step size for subsequent experimental design.

The model deformation is realized by the Morphing function in ANSA. The principle is to create a deformation box. The deformation control of different regions is realized by dividing the box. The control points can be translated, rotated, and slipped along the path according to the user's preferences. Because the Morphing function processes the grid file, the surface continuity of the model can be guaranteed to a certain extent, and the parametric automatic deformation can be realized, which is convenient to cooperate with the large sample space extracted by DOE in this paper. The deformation effect is shown in Fig. 8.

3.2 Agent Model Construction and Optimization

According to the determined range of deformation parameters, 13 factors are sampled, and the level is 10. The initial sample points cannot be extremely few as the initial exploration of space. Considering the subsequent addition of points to improve the efficiency, the number of the first

Table 2 Illustration of deformation parameters

serial number	Variables	parameter range
1	Wind window inclination α	
2	Vehicle Top Tilt β	
3	Cab front width characteristics (4 parameters)	
4	Width characteristics of cab windshield	
4	Height characteristics of the cab (2 parameters)	
5	Cab length characteristics (2 parameters)	
6	Vehicle height	
7	Front overhang	
8	Proximity angle	

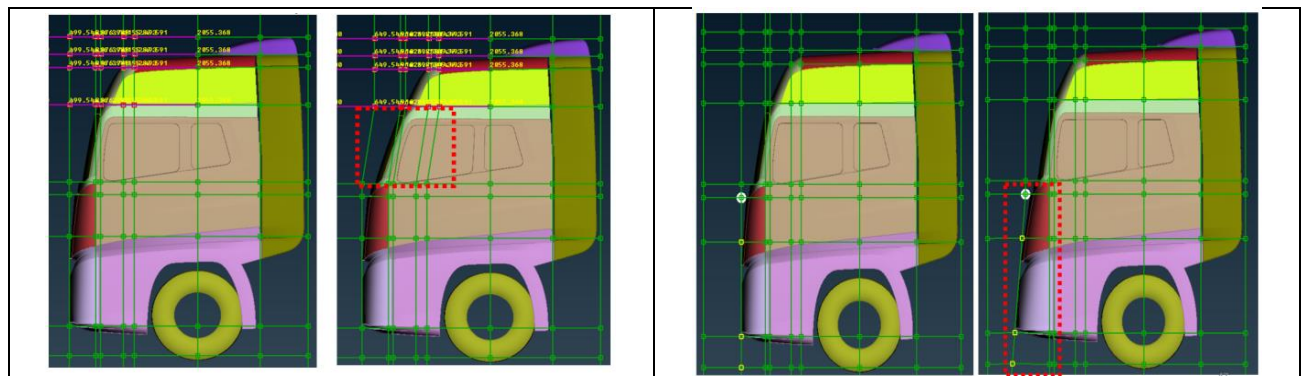


Fig. 8 Morphing Deformation effect diagram

Table 3 Wind tunnel parameters of Tongji University

Nozzle size	6.5m (W)x4.25m(H)	Central mobile belt	7m(L)x1.1m(w)
Nozzle area	27m ²	Wheel rotation unit	330mm (L)x280mm(w)
Length of test section	15m	Fan diameter	8.5m
Rotary center position	4.7m	output power	4000kW
Rotary disc diameter	9m	maximum wind speed	69.4m/s

round of sampling is 66. The optimized Latin square sampling is used to obtain the design matrix of 66 * 13. According to the generated design matrix, parametric automatic deformation can be realized through the OPTIMIZATION module of ANSA, and 66 initial sample models are obtained. Because the stretching and compression of the grid leads to grid quality problems, repairing the grid and replacing the original vehicle model are necessary, which can ensure the consistency of the simulation strategy. The 66 sets of initial examples obtained take the average value of C_D after 2 s, and the results are supplemented to the design matrix, so the sample space with response of 66 * 14 is obtained. Before establishing the surrogate model, the design variables need to be normalized to 0–1. The purpose is to eliminate the dimensional differences of different variables, avoid weight imbalance, and improve the convergence efficiency of the model. Therefore, the most commonly used minimum–maximum normalization is adopted in this paper.

$$x^* = \frac{x - \min(x)}{\max(x) - \min(x)} \quad (12)$$

Among them x is the original data, x^* is the normalized data, and the $\max(x)$ and $\min(x)$ is the minimum and maximum values of the original data.

Next, the initial surrogate model can be constructed, and the response surface and Kriging are selected as the basis of the combined surrogate model. The accuracy of the surrogate model is evaluated by five-fold CV. The evaluation coefficient is R^2 , and the convergence limit η is 0.8. The weight coefficient of the surrogate model is calculated by the PRESS method. The initial sample space is used as a preliminary exploration of the unknown optimization problem. At this time, the accuracy of the surrogate model fails to meet the optimization requirements. Moreover, the local and global mining of the sample space is required, that is, the point-adding strategy of the surrogate model. Local point addition means exploring the space near the optimal value to improve the accuracy of the optimal solution, whereas global point addition is based on the principle of improving the space filling degree to perform global exploration, which can prevent the sample space from falling into local optimum. In this paper, two methods of adding points are selected. The local adding points add the optimal solution of the current surrogate model (given multiple optimal solutions for multiple peaks, add more), and the global adding point strategy adopts the maximum error adding point criterion.

The particle swarm optimization (PSO) algorithm is

used in the optimization algorithm, and the particles with the characteristics of speed, position, and fitness are used to represent the viable solutions of each optimization problem (Ballabio & Vasighi, 2012; Yang et al., 2020). The update formulas of speed and position are as follows:

$$v_i(k+1) = \omega \cdot v_i(k) + c_1 \cdot \text{rand}() \cdot (p_{i\text{best}} - x_i(k)) + c_2 \cdot \text{rand}() \cdot (g_{\text{best}} - x_i(k)) \quad (13)$$

$$x_i(k+1) = x_i(k) + v_i(k+1) \quad (14)$$

In the formula, the velocity and position of the i th particle at the k th iteration are calculated, ω is the inertia weight, c_1 and c_2 are the learning factors, $\text{rand}()$ is a random number in $[0, 1]$, $p_{i\text{best}}$ is the individual extreme value, and g_{best} is the global extremum.

Using different inertia weights at various stages of the evolutionary process can improve the performance of PSO. In this paper, the inertia weight with linear change is used, as shown in the following formula:

$$\omega = (\omega_1 - \omega_2) \times \frac{(\text{MAXITER} - \text{iter})}{\text{MAXITER}} + \omega_2 \quad (15)$$

In the formula, ω_1 and ω_2 are the initial value and the final value of inertia weight respectively, $\omega_1 = 0.9$, $\omega_2 = 0.4$; iter is the current number of iterations; MAXITER is the maximum number of iterations.

In this paper, the learning factor that changes with the number of iterations is used to meet the different needs of the PSO algorithm in different periods, as follows

$$c_1 = (c_{1f} - c_{1i}) \frac{\text{iter}}{\text{MAXITER}} + c_{1i} \quad (16)$$

$$c_2 = (c_{2f} - c_{2i}) \frac{\text{iter}}{\text{MAXITER}} + c_{2i} \quad (17)$$

In the formula, c_{1i} 、 c_{1f} 、 c_{2i} 、 c_{2f} is a constant; iter for the current number of iterations; MAXITER is the maximum number of iterations.

It is found that the algorithm is better when c_{1i} 、 c_{1f} 、 c_{2i} 、 c_{2f} is $c_{1i} = 2.5$ 、 $c_{1f} = 0.5$ 、 $c_{2i} = 0.5$ 、 $c_{2f} = 2.5$ (Ratnaweera et al., 2004). The final optimization flow chart is shown in Fig. 6.

After several rounds of iteration, the accuracy of the final combined surrogate model is $0.812 > \eta$. According to dissimilar styles, different variable ranges are given, and the optimal solution is obtained within their limits. Finally, three optimal solutions are obtained, which represent the lowest wind resistance modeling of flat head models, convex head models, and bullet head models. The three groups of optimal deformation parameters are given Morphing mesh deformation to obtain the cab model. After local detail optimization, the cab simulation is replaced for further verification.

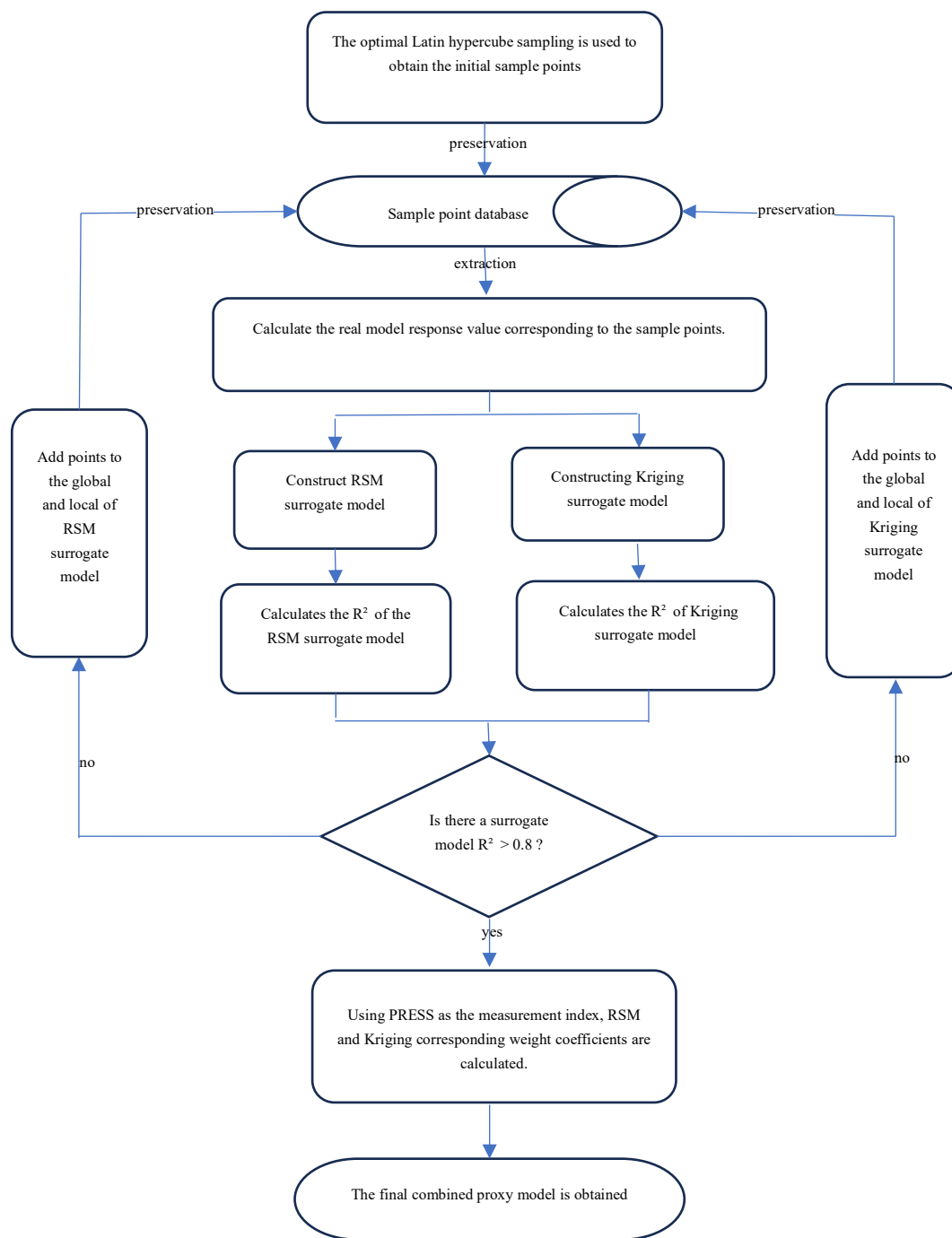


Fig. 9 optimization flow chart

3.3 Results and Some Discussion

Each model is within the boundary limit, and the parameters are optimized to obtain the best match. The comparison results with the predicted values of the surrogate model are within 2%, which proves the reliability of the surrogate model method. The results are further verified by wind tunnel tests. The wind tunnel test was completed in Tongji University Aeroacoustic Wind Tunnel. The Tongji University Wind Tunnel is a 3/4 open-type automotive wind tunnel. The Horiba–Schenck plane measurement force is used to simulate the actual driving road surface through the five-belt system. The specific wind tunnel parameters are shown in Table 3.

In addition to the base model, four cab models, a flathead model, a convex model, a bullet model, and a general-purpose trailer model were made, for a total of five models. Each model shares a set of trailer models. Based on the size of the test section and the length of the whole vehicle, we finally determined the model ratio to be 40%. The model is connected to the balance through the support rod. The four models are arranged, as shown in Fig. 10.

The simulated coefficient of drag and the corrected rate of deviation as well as the rate of drag reduction are shown in Table 4. Due to the different scale of the model used in the test and the simulation model, and the existence of support in the test model, this will make the accuracy of the Reynolds number and resistance deviation. In this

Table 4 Comparison of experimental values and simulation values

	Coefficient of drag C_D		
	simulation value	Deviation rate between simulation value and test value	drag reduction rate
Basic model	0.461	0.98%	-
Flat head models	0.381	1.05%	17.1%
Small convex head model	0.373	0.93%	18.7%
Convex head model	0.351	0.83%	21.7%
Bullet models	0.337	0.90%	27.8%



(a) Flat-top models



(b) Small convex head model



(c) Convex head models



(d) Bullet models

Fig. 10 Wind tunnel test layout

paper, through the method of small-scale model simulation, the test conditions including the support device connected to the balance are restored, and the simulation model is shown in Fig. 10. The corrected deviation of the test data is -0.020, and the deviation of the corrected test values from the simulated values is relatively small, which is around 1%. In the case of the same trailer, the drag

reduction rate of the Small convex head vehicle is 17.1%, the drag reduction rate of the flat head vehicle is 18.7%, the drag reduction rate of the convex head vehicle is 21.7%, and the drag reduction rate of the bullet head vehicle is 27.8%.

The cumulative curve of the drag coefficient is analyzed. The front and bumper of the flat-head vehicle mainly contribute to reducing the drag coefficient. The cumulative drag coefficient is about 0.230, which is 21.8% lower than that of the basic vehicle. The top shape also contributes part of the drag reduction. The cumulative amount of coefficient of drag from the front suspension to the rear

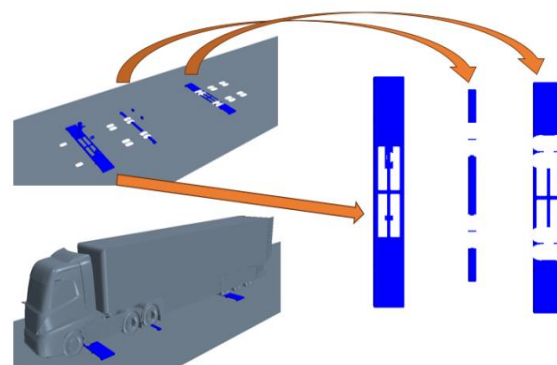
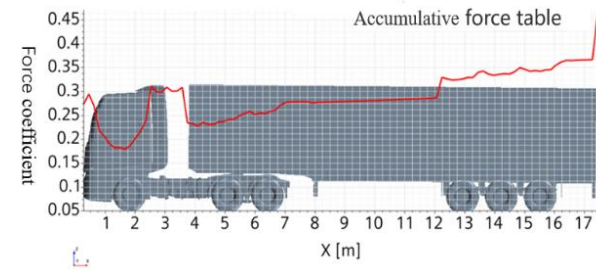


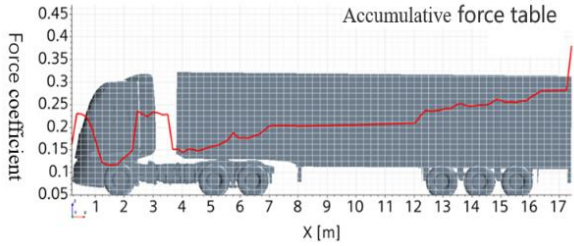
Fig. 11 Benchmark correction simulation model of wind tunnel test

edge of the roof is 0.119, which is 8.5% lower than that of the basic vehicle. For the convex head model, the front wall and the bumper provide the main contribution to reducing the coefficient of drag. The cumulative coefficient of drag is about 0.191, which is 35% lower than that of the basic model. The local trough at the corner of the front wind window is 0.173. The smooth shape of the top also contributes to the good diversion performance, and the coefficient of drag along the front suspension to the roof is reduced by 0.004. For the bullet model, the front and bumper provide the main contribution to reduce the coefficient of drag. The cumulative coefficient of drag is about 0.172, which is 41.5% lower than that of the basic model. The top styling provides excellent airflow guidance. The coefficient of drag along the front suspension to the roof still decreases, which is 51.2% lower than that of the basic model.

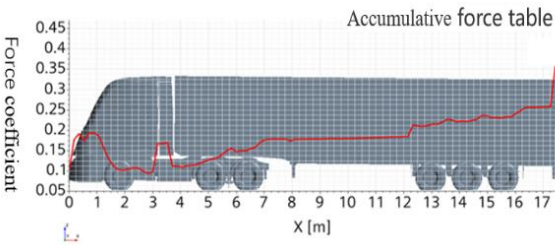
The analysis of the XOZ plane velocity vector diagram of each vehicle type is shown in Fig. 13. The airflow acceleration at the corner of the head is alleviated, and the flow separation on the roof is substantially improved. With the sharpening of the cab shape, the top fillet is extremely smooth, and the high-speed area on the roof is eliminated. The hood optimization moves the large vortex position backward between the body and trailer, reduces incoming



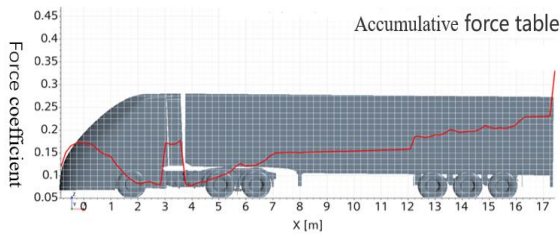
(a)basic model



(b)Flat-top models



(c)Convex head models



(d)Bullet models

Fig. 12 Cumulative curve of coefficient of drag of each model

mass flow, and en-sures tractor-semitrailer continuity. With the decrease of the gap between the cab and the cargo box, the upper air flow of the cargo box has an improved fit, and almost no flow separation is observed at the top of the cargo box of the bullet cab. The optimization of the bottom bumper and other parts reduces the gas mass flow into the lower part of the body and concurrently slows down the airflow velocity flowing through the bottom and reduces the energy loss at the bottom.

Compared with the surface pressure distribution of the YOZ plane cab, the positive pressure area of the windward side of the cab is slightly reduced, the area of the negative pressure area at the corner of the front corner plate and the A-pillar is increased, and the negative pressure extreme value is reduced, indicating that the air flow is smooth and the excessive separation is weakened. The roof fillet and



(a)basic model



(b)Flat-top models

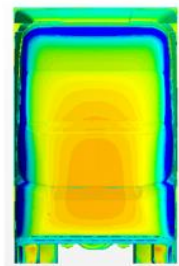


(c)Convex head models

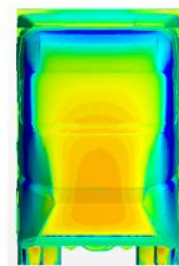


(d)Bullet models

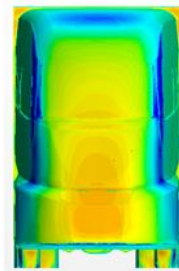
Fig. 13 XOZ plane velocity vector diagram



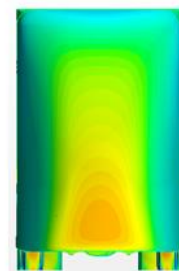
(a)basic model



(b)Flat-top models



(c)Convex head models



(d)Bullet models

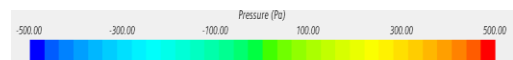


Fig. 14 YOZ plane cab surface pressure distribution map

side fillet transition of the convex head cab are smoother, and the positive pressure area on the windward side is slightly reduced, but the negative pressure area on the side is considerably reduced. Almost no negative pressure is at extreme zone at the edge of the bullet cab, and the airflow is smoothly guided to the side.

In summary, the combination of wind tunnel test and CFD simulation is used in this paper. The automatic deformation of the cab is realized by multivariate

parameterization. The initial sample space is constructed by high-precision simulation strategy to develop the combined surrogate model. The accuracy of the surrogate model is effectively improved by the local and global combination point strategies. Finally, the high-precision combined surrogate model is obtained. The cabs of different styles are obtained by PSO optimization algorithm, and the reliability of the results is verified by wind tunnel tests. The deviation between the final test value and the simulation value is within 1%. The maximum drag reduction rate of the low wind resistance cab is 27.8%. The method in this paper realizes the efficient, low-cost solution of complex CFD optimization problems and proposes a set of efficient solutions to engineering optimization problems. Moreover, it has certain guiding importance for the future development of commercial vehicle styling.

CONCLUSION

1. The complex model preprocessing method, the grid scheme suitable for commercial vehicles, and the physical boundary condition setting in this paper form a set of high-precision CFD simulation calculation strategy for real vehicles. Finally, standard wind tunnel tests are performed, and the error of the corrected result is within 1%.

2. The commercial vehicle cab modeling still has development potential. This paper has an evident drag reduction effect for different modeling styles, and passive rent reduction can be achieved only through the geometric shape change. The maximum drag reduction rate can reach 28%.

3. The combined surrogate model and the composite adding point strategy can effectively improve the accuracy of the surrogate model, fit the high-dimensional optimization problem, and use the optimization in this paper to shorten the design cycle and to save design costs.

CONFLICT OF INTEREST

The authors declare that they have no conflict of interest.

AUTHORS' CONTRIBUTIONS

Genghua Liao and **Xingjun Hu** were in charge of the whole analyses. **Mingxin Xue** and **Lei Yue** wrote the initial manuscript; **Hanbo Yang** and **Peng Guo** assisted with simulation analyses; **Zirui Wang** and **Tongyu Ma** revised the final manuscript. All authors read and approved the final manuscript.

REFERENCE

- Aleksandra, A. R., & Alvin, G. (2022). On the drag reduction of road vehicles with trailing edge-integrated lobed mixers. *Proceedings of the Institution of Mechanical Engineers, Part D: Journal of Automobile Engineering*, 236(7), 1515-1545. <https://doi.org/10.1177/09544070211039697>
- Arabacı, S. K., & Pakdemirli, M. (2023). Aerodynamic improvements of buses inspired by beluga whales. *Journal of Applied Fluid Mechanics*, 16(12), 2569-2580. <https://doi.org/10.47176/jafm.16.12.1694>
- Aultman, M., Wang, Z., & Duan, L. (2021) Effect of time-step size on flow around generic car models. *Journal of Wind Engineering & Industrial Aerodynamics*, 219, 104764. <https://doi.org/10.1016/j.jweia.2021.104764>
- Ballabio, D., & Vasighi, M. (2012). A MATLAB toolbox for self organizing maps and supervised neural network learning strategies. *Chemometrics and Intelligent Laboratory Systems*, 118, 24–32. <https://doi.org/10.1016/j.chemolab.2012.07.005>
- Bates, S., Hastie, T., & Tibshirani, R. (2023). Cross-validation: what does it estimate and how well does it do it?. *Journal of the American Statistical Association*, 119(546), 1434-1445. <https://doi.org/10.1080/01621459.2023.2197686>
- Bayindirli, C. (2021). Reducing of pressure based drag force of a bus model by flow control rod in wind tunnel. *International Journal of Automotive Science and Technology*, 5(4), 412-418. <https://doi.org/10.30939/ijastech.994351>
- Davis, S. C., & Boundy, R. G. (2022). *Transportation energy data book*. Edition 40. Oak Ridge National Laboratory (ORNL), Oak Ridge, TN (United States). <https://doi.org/10.2172/1767864>
- Farghaly, M. B., Sarhan, H. H., & Abdelghany, E. S. (2023). Aerodynamic performance enhancement of a heavy trucks using experimental and computational investigation. *CFD Letters*, 15(3), <http://doi.org/10.37934/cfdl.15.8.7394>
- Garcia-Ribeiro, D., Bravo-Mosquera, P. D., Ayala-Zuluaga, J. A., Martinez-Castañeda, D. F., Valbuena-Aguilera, J. S., Cerón-Muñoz, H. D., & Vaca-Rios, J. J. (2023). Drag reduction of a commercial bus with add-on aerodynamic devices. *Proceedings of the Institution of Mechanical Engineers, Part D: Journal of Automobile Engineering*, 237(7), 1623-1636. <https://doi.org/10.1177/09544070221098209>
- Kim, S. H., & Kim, J. J. (2023). Study on drag reduction of commercial vehicle using flow control device. *Journal of the Korean Society of Visualization*, 21(2), 8–13. <https://doi.org/10.5407/JKSV.2023.21.2.008>
- Levin, J., & Chen, S. H. (2023). Aerodynamic of a refrigerated truck and improvement to reduce its aerodynamic drag. *Proceedings of the Institution of Mechanical Engineers, Part D*. <https://doi.org/10.1177/09544070221113128>
- Lv, L. Y., Lu, Y. J., Wang, S., et al. (2019). Agent model technology and its application: current situation and prospect. *Chinese Journal of Mechanical Engineering*, 60(3), 254-281. <https://dx.doi.org/10.3901/JME.2024.03.254>.
- McAuliffe, B. R., Ghorbanishohrat, F., & Barber, H. (2022). *Preliminary investigation towards next generation truck design for aerodynamic efficiency*. Techni Cal Report, National Research Council of Canada. Aerospace, Artwork Size. www.https://nrc-publications.canada.ca/eng/view/object/?id=610b10b1-805a-4047-a908-174b18a0ea07

- McKay, M. D., Beckman, R. J., & Conover, W. J. (2000). A comparison of three methods for selecting values of input variables in the analysis of output from a computer code. *Technometric*, 42(1), 55-61. <http://dx.doi.org/10.1080/00401706.2000.10485979>
- Mohamed-Kassim, Z., & Filippone, A. (2010). Fuel savings on a heavy vehicle via aerodynamic drag reduction. *Transportation Research Part D: Transport and Environment*, 15(5), 275-284. <https://doi.org/10.1016/j.trd.2010.02.010>
- Nagelkerke, N. J. (1991). A note on a general definition of the coefficient of determination. *Biometrika*, 78(3), 691-692. <https://doi.org/10.2307/2337038>
- Ratnaweera, A., Halgamuge, S. K., & Watson, H. C. (2004). Self-organizing hierarchical particle swarm optimizer with time-varying acceleration coefficients. *IEEE Transactions on Evolutionary Computation*, 8(3), 240-255. <https://doi.org/10.1109/TEVC.2004.826071>
- Schiavo, D., Trevizan, L. C., Pereira-Filho, E. R., & Nóbrega, J. A. (2009). Evaluation of the use of multiple lines for determination of metals in water by inductively coupled plasma optical emission spectrometry with axial viewing. *Spectrochimica Acta Part B: Atomic Spectroscopy*, 64(6), 544-548. <https://doi.org/10.1016/j.sab.2009.05.009>
- Wang, J. Y., Geng, Y. L., Hui, Z., Li, T. H., Liu, Z. C., Li, J. C., Hu, X. J. (2020). Research on drag reduction of square-backed vehicle model based on plasma flow control. *Automotive Engineering*, 42 (6), 753-758. <https://doi.org/10.19562/j.chinasae.qcgc.2020.06.007>
- Wang, Y., Wu, C., Tan, G., & Deng, Y. (2017). Reduction in the aerodynamic drag around a generic vehicle by using a non-smooth surface. *Proceedings of the Institution of Mechanical Engineers, Part D: Journal of Automobile Engineering*, 231(1), 130-144. <https://doi.org/10.1177/0954407016636970>
- Wiedemann, J. (1996). The influence of ground simulation and wheel rotation on aerodynamic drag optimization-potential for reducing fuel consumption. *SAE Transactions*, 810-819. <https://doi.org/10.3354/cr030079>
- Willmott, C., & Iatsuura, K. (2005) Advantages of the mean absolute error (MAE) over the root mean square error (RMSE) in assessing average model performance. *Climate Research*, 30(1)79-82. <https://doi.org/10.3354/cr030079>
- Yadegari, M., & Bak Khoshnevis, A. (2021). Numerical and experimental study of characteristics of the wake produced behind an elliptic cylinder with trip wires. *Iranian Journal of Science and Technology, Transactions of Mechanical Engineering*, 45, 265-285. <https://doi.org/10.1007/s40997-020-00373-6>
- Yadegari, M., Bak Khoshnevis, A., & Boloki, M. (2023). An experimental investigation of the effects of helical strakes on the characteristics of the wake around the circular cylinder. *Iranian Journal of Science and Technology, Transactions of Mechanical Engineering*, 47(1), 67-80. <https://doi.org/10.1007/s40997-022-00494-0>
- Yang, W. Y., Cao, W., Kim, J., Park, K. W., Park, H. H., Joung, J., & Im, T. (2020). *Applied numerical methods using MATLAB*. John Wiley & Sons. <https://doi.org/10.5860/choice.43-1615>
- You, D., & Moin, P. A. (2009). Dynamic global coefficient subgrid-scale model for large-eddy simulation of turbulent scalar transport in complex geometries. *Physics of Fluids*, 21(4). <https://doi.org/10.1063/1.3115068>
- Zhang, Y. C., Zheng, Z. Y., Wu, K. G., & Zhang, Z. (2020). Research on active drag reduction of MIRA fast back model. *Automotive Engineering*, 42 (5), 588-592. <https://doi.org/10.19562/j.chinasae.qcgc.2020.05.004>